Soft Matter

Accepted Manuscript

This is an *Accepted Manuscript*, which has been through the Royal Society of Chemistry peer review process and has been accepted for publication.

Accepted Manuscripts are published online shortly after acceptance, before technical editing, formatting and proof reading. Using this free service, authors can make their results available to the community, in citable form, before we publish the edited article. We will replace this *Accepted Manuscript* with the edited and formatted *Advance Article* as soon as it is available.

You can find more information about *Accepted Manuscripts* in the Information for Authors.

Please note that technical editing may introduce minor changes to the text and/or graphics, which may alter content. The journal's standard Terms & Conditions and the Ethical guidelines still apply. In no event shall the Royal Society of Chemistry be held responsible for any errors or omissions in this *Accepted Manuscript* or any consequences arising from the use of any information it contains.

ROYAL SOCIETY OF CHEMISTRY

www.rsc.org/softmatter

GRAPHIC ABSTRACT

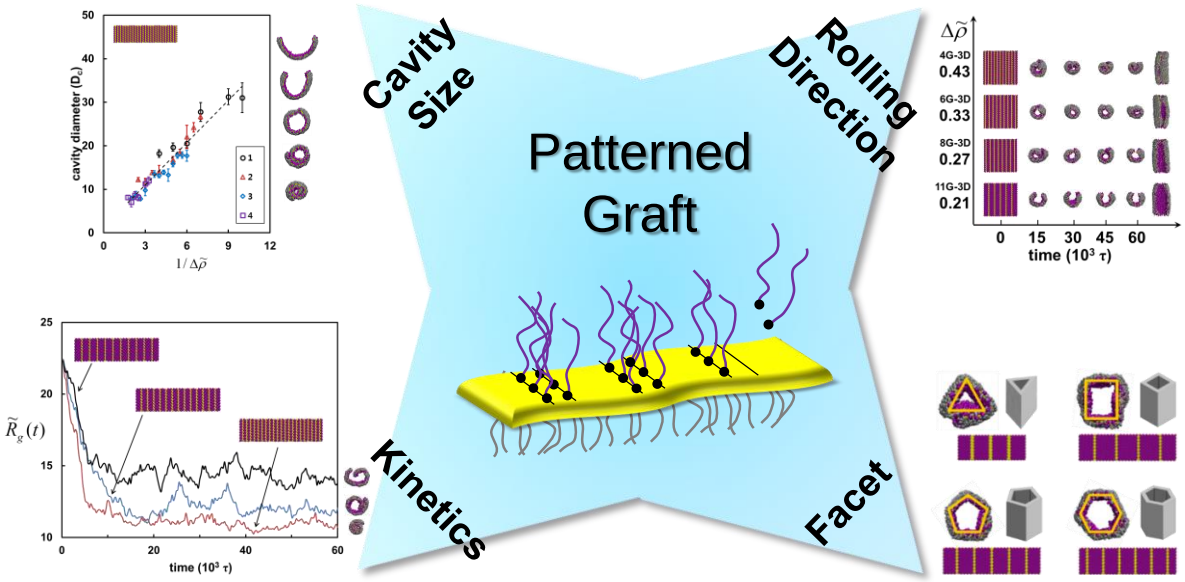

By patterning surface grafts, two-dimensional grafted sheets are programmed to self-roll into hollow tubes with a desired cavity size, direction, kinetics and faceted forms.

Self-Rolled Nanotubes with Controlled Hollow Interiors by Patterned Grafts

*Minwoo Han, Jungin Hyun and Eunji Sim**

Department of Chemistry and Institute of Nano-Bio Molecular Assemblies, Yonsei University,

50 Yonsei-ro Seodaemun-gu, Seoul 120-749 Korea

esim@yonsei.ac.kr

RECEIVED DATE (to be automatically inserted by the publisher)

ABSTRACT By patterning surface grafts, we propose a simple and systematic method to form tubular structures for which two-dimensional grafted sheets are programmed to self-roll into hollow tubes with a desired size of the internal cavity. Repeating pattern of grafts utilizing defect sites causes anisotropy in the surface-grafted nanosheet, which spontaneously transforms into a curved secondary architecture and, thus, becomes a potential tool with which to form and control the curvature of nanotubes. In fact, the degree and the type of graft defect allow control of the internal cavity size and shape of the resulting nanotubes. By performing dissipative particle dynamics simulations on coarse-grained sheets, we found that the inner cavity size is inversely proportional to the graft-defect density, the difference in the graft densities between the two surface sides of the layer, regardless of whether the defects are patterned or random. While a random distribution of defects gives rise to a non-uniform local curvature and often leads to twisted tubes, regular patterns of graft defects ensure uniform local curvature throughout the sheet, which is important to generate monodisperse nanotubes. At a low graft-defect density, the sheet-to-tube transformation is governed by the layer anisotropy, which induces spontaneous scrolling along

* Corresponding author. Email-address: esim@yonsei.ac.kr, Fax: +82-2-364-7050.

the long edge of the sheet, resulting in short tubes. Thus, the curve formation rate and the cavity diameter are independent of the pattern of the graft defects. At a high graft-defect density, however, the scroll direction owing to the graft pattern may conflict with that due to the layer anisotropy. To produce monodisperse nanotubes, two factors are important: (1) a graft-defect pattern parallel to the short edge of the layer, and (2) a graft-defect area wider than half of the graft coil length.

I. INTRODUCTION

The nanotube has attracted considerable interest as a potential, cutting-edge material, as it has diverse functionalities depending on the structural properties and characteristics of its constituents. Therefore, hollow secondary types of architecture including organic microtubes[1] and nanotubes (such as graphene[2] and carbon nanotubes[3]) have been studied experimentally[1-11] and theoretically.[12-14] The size of the internal cavity is one of the most interesting characteristics of nanotubes because a hollow interior enables potential applications in nanotechnology including medical and industrial encapsulation.[3-5] For instance, adjusting the amount of a delivered encapsulant is a simple matter of changing the number of dispensing tubes. Properties such as the time-release profile or the cell membrane penetration efficiency are expected to depend intimately upon the shape of the delivery vehicle, for instance, the tubule length and the internal cavity diameter.[6, 15] Structural parameters also govern the particle mean deposition distance. Therefore, regulation of the size and/or the cross-sectional shape of the hollow interior would be crucial for applications.[7, 8, 16]

Various fabrication methods of hollow nanotubes have been developed using a range of materials, including organic polymers[17] and metal oxides.[18] Among them, self-assembly[18-22] and template-based methods[17, 23-26] and related building block materials have been intensively investigated. These methods, however, have several drawbacks. Template-based methods have to resolve issue of the preparation and removal of the templates. Self-assembly processes must deal with polydispersity of the

tubes. Another potential approach is to employ anisotropic bilayers composing of inorganic[27-29] or organic[30] layers with contrasting properties either intrinsically or externally. Because the layer anisotropy governs the curvature, i.e., the size of the internal cavity, control of the internal cavity of such bilayers is accomplished by varying the constituents.[13] It is certainly more feasible if the degree of sheet anisotropy can be scaled systematically and readily without the need to prepare different types of bilayers. Recently, the formation of a spontaneous curvature by means of a surface graft modification method was demonstrated.[31, 32] Dissipative particle dynamics (DPD) simulations showed that a broken volume and chemical symmetry of the surface grafts can be used to control the size of the internal cavity by transforming two-dimensional sheets into cylindrical structures.[31] Even when the surface is grafted with identical coils, anisotropy can arise due to asymmetric graft configurations, leading to the formation of a hollow tube.[32, 33] Therefore, we envision that alteration of the properties of the surface grafts is a promising and scalable means of practically and methodically tuning the size of the internal cavities of nanotubes.

Surface-modified organic sheets can be fabricated successfully by polymer brush techniques involving, for instance, grafted graphene sheets.[34] By utilizing radical polymerization, the stable and controllable formation of grafted polymer surfaces becomes practical. Nonetheless, graft defects are inevitable during such fabrication processes, leading to anisotropic sheets to varying degrees. Patterned defect formation by means of chemical lift-off lithography was also successfully realized.[34] Numerous nanolithography methods has been developed and utilized for fabricating nanometer-scale semiconductor integrated circuits and nanoelectromechanical systems.[31] In particular, complicated nano-pattern fabrication is now readily available if using nanoimprinting,[35, 36] dip-pen,[36, 37] nanosphere lithography[38] and other such methods. In general, these methods are used to modify two-dimensional surface structures. Only recently have certain nanolithography techniques been applied for the fabrication of complex three-dimensional nanostructures by tailoring the shape of two-dimensional sheet-like structures.[31] Such technical advances provide clues about controlling nanoscale systems more accurately. Nevertheless, these methods are often time-consuming and require many fabricating steps.

Therefore, despite their fascinating outlook, problems remain before practical applications of nanostructure fabrication for mass production and reliable reproducibility can be achieved and, for that reason, insights based on simulations will play a pivotal role to achieve such goals.

In this work, we introduce and extend the usage of the two-dimensional surface modification technique to manipulate a three-dimensional shape consisting of polymer sheet moieties as a simple and highly reproducible fabrication method for nanotubes. It is clear that fabricating a two-dimensional surface is more feasible than fabricating a three-dimensional surface. Therefore, obtaining controlled three-dimensional self-roll programmed nanotubes by means of the two-dimensional fabrication of a polymer sheet surface will represent an excellent and practical advance in the area of three-dimensional architecture formation. We focus on how graft defects can be utilized to control the fabrication of a hollow tube by performing DPD simulations on various graft-defect model systems. We thoroughly examine the role of defect densities and control of the curvature with respect to the graft density difference and the pattern of defects. This article is organized as follows. Section II describes coarse-grained sheet model along with a brief explanation of the dissipative particle dynamics. Potential parameters and computation details are also presented in Section II. Section III discusses the formation of hollow nanotubes with various types of graft defect models. The method used to control the internal cavity diameter, scroll direction, and kinetics is also presented. Concluding remarks appear in Section IV.

II. MODEL AND METHODOLOGY

Here, surface-grafted coarse-grained flexible nanosheets are modeled, as depicted in Scheme 1. The coarse-grained model is advantageous because it replaces a group of atoms with a single bead, enabling highly efficient computations compared to all-atom molecular dynamics (MD) simulations by roughly 10^4~10^7 times.[39]

As shown in Scheme 1(a), a well-ordered two-dimensional bare nanosheet was prepared by bonding layer beads in both the lateral and longitudinal directions. Each of the bonded i^{th} and j^{th} beads at a distance of r_{ij} are connected by a harmonic spring, $\mathbf{F}_{ij} = -k(r_{ij} - \bar{r})\hat{r}_{ij}$, with force constant k and equilibrium distance $\bar{r}$ corresponding to the bead types and bonding schemes. We applied an identical force constant and a bond length for both directions in order to prevent layer anisotropy which may have arisen due to the bonding anisotropy of the layer beads. To model flexible nanolayers and graft coils, no angle constraint was applied between the beads.

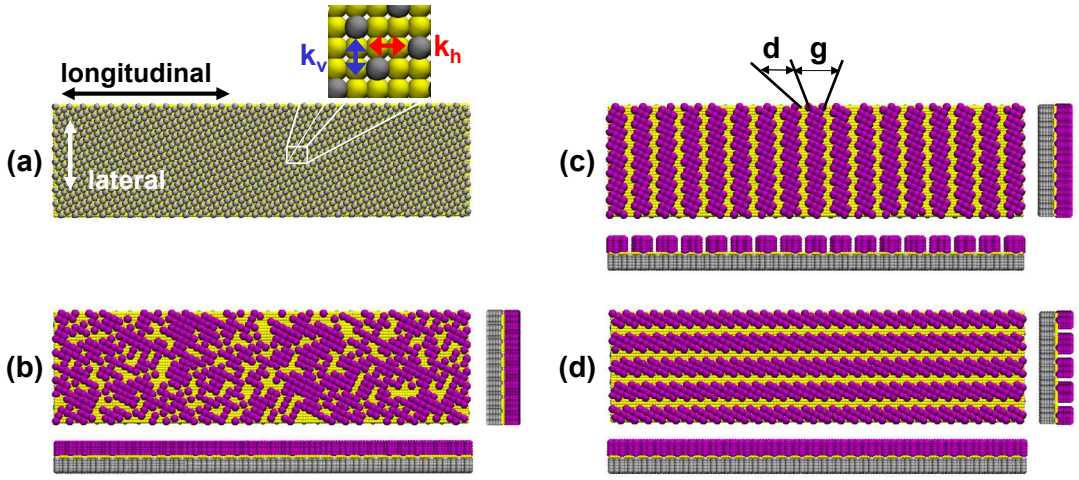

Scheme 1. Top and side views of the initial graft models of a rectangular nanosheet along with the layer-bead (yellow beads) arrangement and their bonding scheme. (a) ***R***-coil (reference side, gray beads) grafts and ***D***-coil (defect side, purple beads) grafts of (b) random point defects (Model RP), (c) patterned vertical line defects (Model PL-V), and (d) patterned horizontal line defects (Model PL-H). For (b) to (d), the graft-defect density, $\Delta\tilde{\rho} = 0.32$, was chosen for illustration. As shown in (c), the notation *g*G-*d*D denotes the repeating pattern consisting of *g* grafted points followed by missing *d* graft points.

To explore the shape effect, we built two types of nanolayers: a square (80×80) layer and a rectangular (40×150) layer. The two surface sides of the bare nanosheet were then grafted with linearly connected five-bead chains. We chose graft points in a hexagonal arrangement to prevent overcrowding of the graft coils, as shown in Scheme 1(a). On the reference side, graft coils are attached onto all graft points such that the graft density $\tilde{\rho}_R = n_G / n_{tot} = 1$, where n_{tot} is the total number of graft points and n_G is the number of grafted coils. On the defect side, whereas the graft points and graft coils are identical to the reference side, a number of grafted coils are removed depending on the graft density, $0 \le \tilde{\rho}_D \le 1$. The graft-defect density of the nanosheet is then defined as the difference in the graft density between the reference and the defect sides, as $\Delta\tilde{\rho} = \tilde{\rho}_R - \tilde{\rho}_D$. The graft coils on the reference surface are referred to as ***R***-coils (symbol ***R***, gray beads), and those on the defect side are called ***D***-coils (symbol ***D***, purple beads), while ***N*** and ***S*** denote, respectively, the nanolayer (yellow beads) and the solvent beads (omitted from the images throughout the manuscript for clarity of the illustrations).

We employed point defect models and line defect models to study the role of the graft-defect density on the secondary architecture. For instance, Model RP denotes random point defects, with the defects distributed randomly. Model PL-H (PL-V) denotes patterned horizontal (vertical) line defects that are parallel to the longitudinal (lateral) direction of the sheet. For notations, we use *g*G-*d*D to denote a patterned line defect model, where the repeating pattern consists of *g* grafted lines followed by missing *d* graft lines, where the layer beads are exposed to a solvent, along the line of layer beads. For instance, Schemes 1(c) and (d) correspond to the 6G-3D pattern. The patterned graft is useful because the cavity diameter of the resulting structures and overall kinetics are robust, while details of the trajectory may slightly change with respect to the simulation conditions such as initial velocity distributions or bead positions. For each *g*G-*d*D pattern, we examined various simulation conditions and confirmed that the self-rolling trajectory presented here is not a special case among an ensemble of different trajectories but is a repetitive and representative outcome. For random models, however, trajectories vary significantly

depending on the random defect distribution so that an ensemble of at least three uncorrelated initial defect distributions were constructed and simulated for a given defect condition.

For morphology transformation in a condensed phase, such as in a solid state or a solution, the hydrodynamic effect is one of the critical factors. Thus, we used the DPD method on surface-grafted coarse-grained sheets to study the role of the graft-defect density. The fundamentals of the DPD algorithm are based on molecular dynamics. In addition to the conservative force ($\mathbf{F}_{ij}^{C}$), however, the total force on a particle i ($\mathbf{F}_i$) in the DPD method includes the dissipative force ($\mathbf{F}_{ij}^{D}$) and the random force ($\mathbf{F}_{ij}^{R}$) acting between the i^{th} particle (at $\mathbf{r}_i$ with the velocity $\mathbf{v}_i$) and the j^{th} particle (at $\mathbf{r}_j$ with $\mathbf{v}_j$) such that[40,39]

$$\mathbf{F}_i = \sum_{i \neq j} \left(\mathbf{F}_{ij}^{C} + \mathbf{F}_{ij}^{D} + \mathbf{F}_{ij}^{R} \right) \tag{1}$$

$$\mathbf{F}_{ij}^{C} = a_{ij}(1 - r_{ij}/r_c)\hat{r}_{ij} \tag{2}$$

$$\mathbf{F}_{ij}^{D} = -\gamma(1 - r_{ij}/r_c)^2(\hat{r}_{ij} \cdot (\mathbf{v}_i - \mathbf{v}_j))\hat{r}_{ij} \tag{3}$$

$$\mathbf{F}_{ij}^{R} = \sigma(1 - r_{ij}/r_c)\zeta_{ij}\Delta t^{-1/2}\hat{r}_{ij} \tag{4}$$

where $r_{ij} = \left| r_{ij}\hat{r}_{ij} \right| = \left| \mathbf{r}_i - \mathbf{r}_j \right| \leq r_c$, with $r_c = 1.0$ being the cutoff distance. Various parameters are used to control the interaction between DPD beads: a_{ij} represents the repulsion strength between particles i and j; the dissipation strength $\gamma = 4.5$; and the random noise strength $\sigma = 3.0$ to control the temperature,[41] as $\sigma^2 = 2\gamma k_B T$. Δt is the propagation time step and ζ_{ij} is a Gaussian random number with zero mean and unit variance.[39] The DPD method is discussed briefly here, but the details of the method can be found in the literature.[31, 32, 41]

All DPD simulations were performed with the LAMMPS package[42] with a time step $\Delta t = 0.04\tau$ and with the temperature maintained at 0.3 in DPD reduced units.[39] VMD was used for visualization.[43] For all simulations presented here, the periodic boundary condition was applied to all directions. A rectangular surface-grafted sheet is placed inside a simulation box ($80 \times 40 \times 40$, reduced unit) which is

filled with single-bead solvents. The total number of beads in the simulation box is 384,000 (the number density of the system, $\rho = 3$) including the solvent beads. For a square sheet, a $60 \times 60 \times 50$ box containing 540,000 beads (again, $\rho = 3$) was used. The bead number density in DPD simulation is chosen as $\rho = 3$ to satisfy the scaling relation between the repulsion parameter and the system density.[41] The DPD potential parameters used for the models are listed in Table 1. Note that all repulsive potential parameters are 25 except for $a_{N\alpha}$, which is 30. Thus, the solvent is a theta solvent to coils, whereas the layer beads are relatively repulsive to other types of beads. Hence, assuming that the solvent is water, the layer may be regarded as hydrophobic and the graft coils as hydrophilic.

Table 1. DPD potential parameters: repulsion parameter ($a_{\alpha\beta}$), bonding force constant (k), and equilibrium bond distance ($\bar{r}$). In subscripts *N*, *R*, *D*, and *S* represent, respectively, the nanolayer, reference and defect coil, and the solvent beads. $a_{\alpha\beta}$ is in units of $k_B T$.

graft coil					Nanolayer			
$a_{\alpha\alpha}$ $(\alpha = R,D,S)$	a_{RS}	a_{DS}	k_{coil}	$\bar{r}_{coil}$	$a_{N\alpha}$ $(\alpha = R,D,S)$	a_{NN}	k_{sheet}	$\bar{r}_{sheet}$
25	25	25	25	0.5	30	25	50	0.5

III. RESULTS AND DISCUSSION

Figure 1(a) presents the defect-free grafted nanosheet for which coils are attached at all graft points on both sides of the layer; *i.e.*, $\tilde{\rho}_R = \tilde{\rho}_D = 1$. Whereas bare lyophobic sheets fold and crumple to avoid contact with the solvent beads, the defect-free grafted sheets ($\Delta\tilde{\rho} = 0$) undulate with sinuous movements in time, akin to a fluctuating flat membrane, and they never scroll into tubes or rolls. Lyophilic surface grafts spread into the solvent and prevent the sheet from collapsing owing to their

entropic repulsion. Rectangular sheets, however, always have curvature in the longitudinal direction in order to reduce the stress caused by the anisotropic shape. In contrast, graft-defect nanosheets scroll into tubular structures, often with a hollow internal cavity, where ***D***-coils on the defect surface always form in the interior due to the entropy. Figures 1 and 2 show that, regardless of the type of defect models or the aspect ratio of the layer, as the graft-defect density increases, the sheets roll up more and eventually transform into tubes. The structures obtained from random defects, Model RP, in Fig. 1, clearly exhibit irregular local curvatures and patterned defects, while Model PL, in Fig. 2, produced relatively uniform local curvatures. Therefore, we envision that manipulation of the graft-defect pattern is a potentially useful tool for systematically forming hollow nanotubes with controlled interiors.

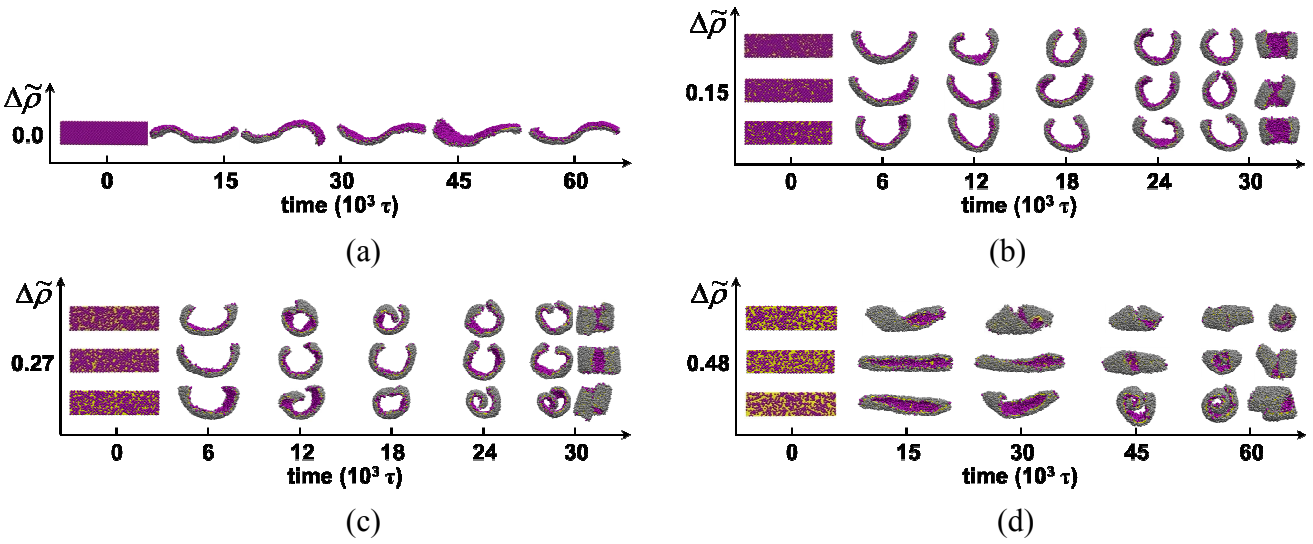

Figure 1. Initial grafts and time evolution of the spontaneous curvature formation of 4:15 rectangular nanosheets at various graft-defect densities, $\Delta\tilde{\rho}$. The defect-free nanosheet in (a) and the random point defect models (Model RP) in (b) are shown, with $\Delta\tilde{\rho} = 0.15$ (c) $\Delta\tilde{\rho} = 0.27$, and (c) $\Delta\tilde{\rho} = 0.48$. In the initial grafts, purple points represent coil grafted points, while yellow layer beads are exposed at defect sites. At other time points, cross-sectional views of the sheet are shown. For a given $\Delta\tilde{\rho}$, three uncorrelated randomly distributed defect models were chosen.

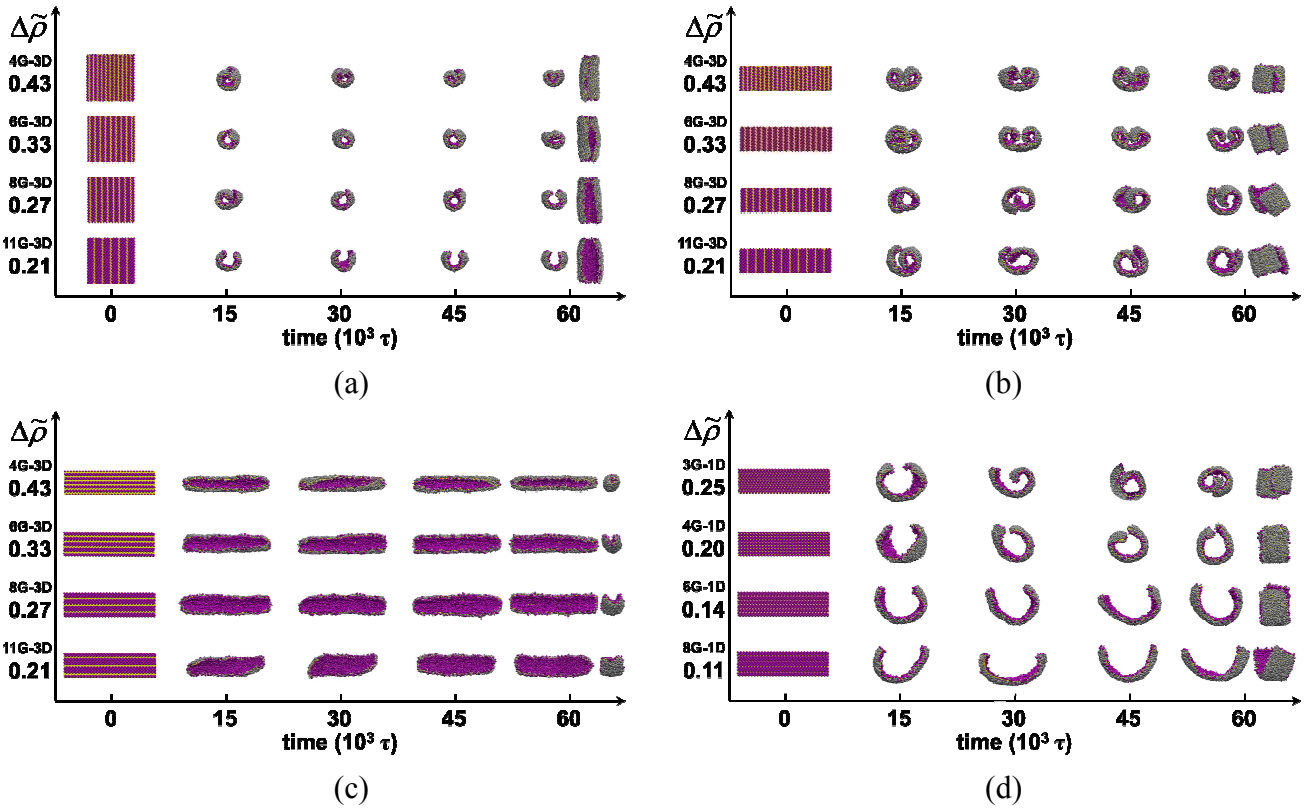

Figure 2. Initial graft patterns and cross-sectional views of the evolving tubes with line defect models. (a) *g*G-3D pattern of a square nanosheet, *g*G-3D patterns of (b) Model PL-V and (c) Model PL-H of a rectangular nanosheet. (d) *g*G-1D pattern of Model PL-H of a rectangular nanosheet. In the initial grafts, purple points denote coil grafted sites, while yellow layer beads are exposed at the defect sites.

A. Cavity Size

A graft defect is inevitable when constructing surface grafted polymer sheets, and Figs. 1 and 2 demonstrate that a greater graft-defect density, $\Delta\tilde{\rho}$, leads to a smaller internal cavity. A quantitative comparison is presented in Fig. 3 in which, for all defect models considered here, the size of the internal cavity and the graft-defect density are strongly correlated. The cavity diameter, D_c, is inversely proportional to $\Delta\tilde{\rho}$. In particular, the cavity diameter of Model PL-V in Fig. 3(a) fits the linear regression well as a function of the reciprocal graft-defect density, $1/\Delta\tilde{\rho}$, as the regular pattern of line

defects induces a uniform curvature over the entire sheet. The cavity diameters for the random point defect models in Fig. 3(b), however, vary rather greatly among the cases at a given $\Delta\tilde{\rho}$. The slope in Fig. 3(d) is steeper than those in Figs. 3(a) to (c) owing to the shape of the nanosheet. Whereas the slopes of the rectangular sheets in Fig. 3(a) to (c) are roughly equal, the slope of the square sheet is

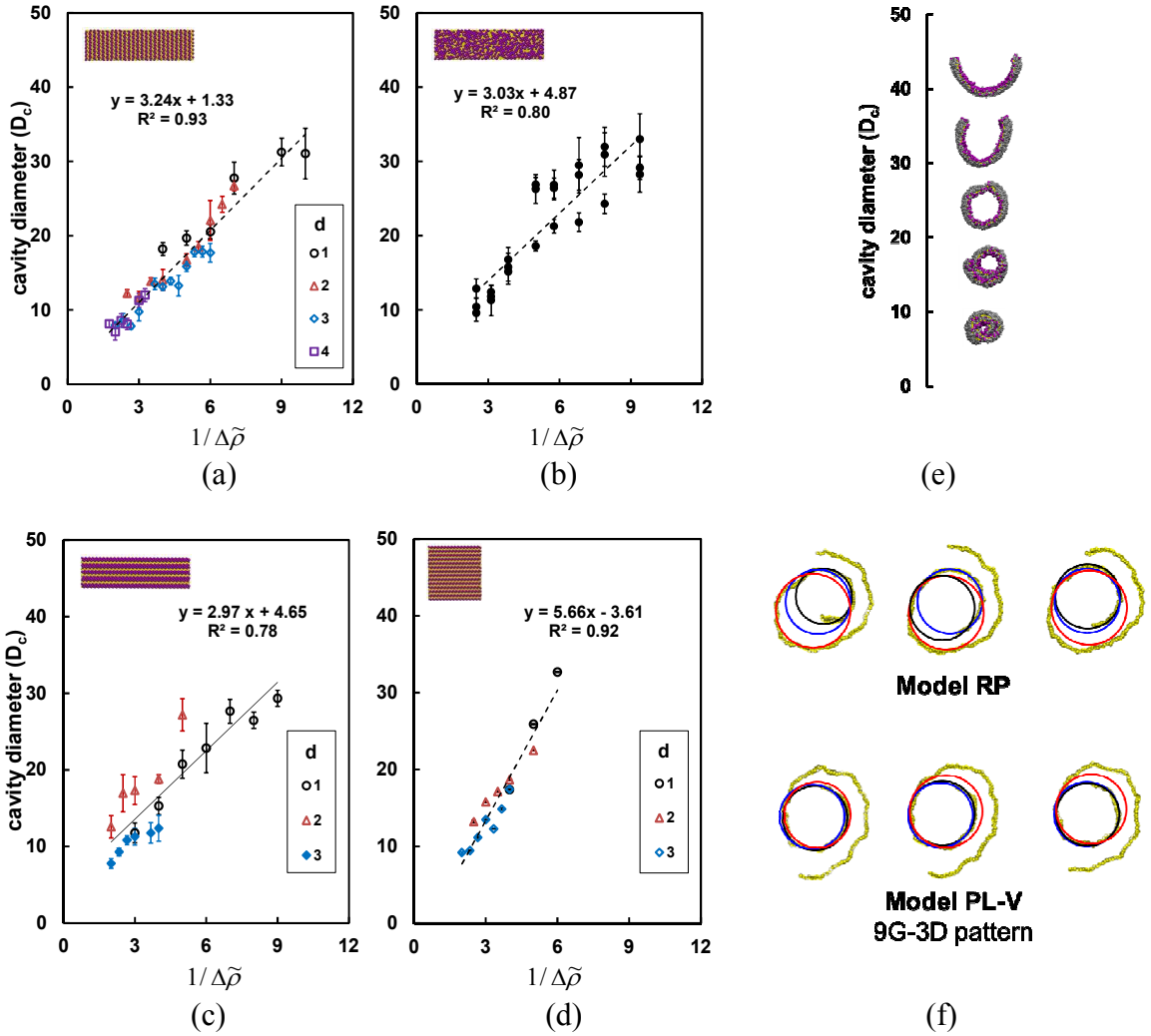

Figure 3. Relationship between the graft-defect density ($\Delta\tilde{\rho}$) and the cavity diameter (D_c): (a) Model PL-V, (b) Model RP, and (c) Model PL-H of a rectangular nanosheet, (d) Model PL of a square nanosheet. Here, (e) visualizes the relationship between D_c and the cross-section of the nanotubes. Schematically, (f) shows how to determine the average and the standard deviation of the cavity

diameter, e.g., when $\Delta\tilde{\rho} = 0.25$. Values in legends are d values of the gG-dD defect models.

nearly twice that of the rectangular sheets. Note that, for Model PL-H, the rolling direction of the graft-defect pattern (along the lateral direction) and that of the anisotropic layer (along the longitudinal direction) conflict with each other. Thus, we denoted data points in Fig. 3(c) according to two types of markers depending on the shape of the resulting nanotubes. Hollow markers represent short tubes (resulting from the rolling along the longitudinal direction of the layer), and solid markers denote long tubes (resulting from the rolling along the lateral direction of the layer). In addition, all of the PL-H gG-2D patterns produced twisted tubes owing to this conflict. Due to the mixed formation of long, short, and twisted tubes, the linear regression fit of Model PL-H in Fig. 3(c) is even poorer than that of the random point defect model in Fig. 3(b), which implies that control of the rolling direction is critical for a monodisperse formation of nanotubes. This also indicates that the degree of variation of the cavity diameter is governed not only by the shape and the size of the layer but also by the graft-defect pattern. Control of the cavity diameter and the formation of monodisperse nanotubes become feasible when the rolling direction of the graft defect and that of the layer coincide, as in Model PL-V for instance. As shown in Fig. 3(f), the cavity diameter was measured as the average of the three projected circles that match the local curvature of the inner cavity. Therefore, the small error bars represent the uniformity of the local curvature, leading to circular cylindrical tubes, whereas the large error bars represent irregularly shaped tubes. Details of the relationship between the rolling direction and the type of defect pattern and manipulation of the scroll direction are discussed further in the following section.

Figure 4 presents the cavity diameter with respect to the structural aspects of the gG-dD pattern for Models PL-V and PL-H. For both models, as shown in Figs. 4(a) and (c), the cavity diameter varies linearly with the graft width, g. The narrow defect width (for $d < 3$) gives rise to steeper slopes, representing drastic changes in the curvature with respect to the graft width g, as $1/\Delta\tilde{\rho}$ varies with g noticeably. The wider defect models, for instance at $d \geq 3$, however, become less sensitive to a change of graft width such that varying the defect width causes little change. While this finding is in good

agreement with Fig. 3, it also suggests, when the defect area is relatively wide, that the cavity size is mainly governed by the width of the defect area, not only by the graft-defect density.

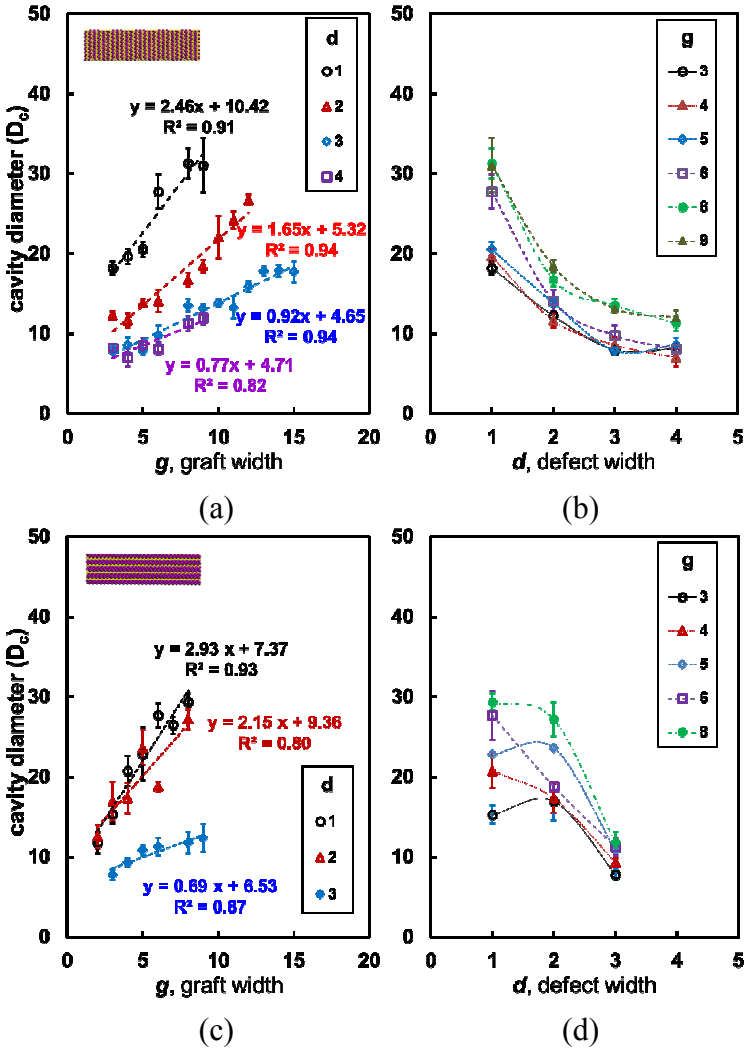

Figure 4. The cavity diameter as a function of the graft width, *g*, and the defect width, *d*. (a) and (b) denote the *g*G-*d*D pattern of Model PL-V, and (c) and (d) denote this for Model PL-H.

The indistinguishable *g*G-3D and *g*G-4D models clearly demonstrate that the grafted sheets folded, rather than bent, at the wide defect area because the lyophobic layer avoids energetically unfavorable contact with the solvent beads. Fig. 4(b) shows an inverse relationship between the cavity diameter and the defect width *d*. The *g*G-*1*D patterns show noticeable change in the cavity diameter with respect to the graft width. In other words, narrow defect patterns are suitable for producing hollow tubes with a

wide range of systematically varying cavity diameters, whereas it should be easier to produce monodisperse nanotubes when wide defect patterns are used. While the structural parameters have a simple relationship with the cavity diameter, the proportionality constant depends on the type of graft-defect pattern. Again, the linear regression fit of Model PL-H exhibits relatively poor correlation due to the mixed rolling direction.

B. Rolling Direction

Figure 3(c) demonstrates, when producing monodisperse nanotubes with a systematic cavity size when an anisotropic shape layer is employed, that control of the scroll direction is also important. In this work, the relationship between the pattern and the scroll direction is determined by examining the two types of defect pattern models on anisotropic layers. For Model RP, the layer anisotropy always governs the scroll direction regardless of the graft defect range of $0.10 \le \Delta\tilde{\rho} \le 0.48$. For Model PL, however, the sheet tends to bend perpendicular to the direction of the line defects to hide lyophobic layer beads efficiently that are exposed due to the graft defects. The defect pattern of Model PL-V promotes scrolling along the longitudinal direction, in good agreement with the scroll direction according to the anisotropic shape of the layer, *i.e.*, a rectangle. Therefore, all vertical defect patterns in Fig. 3 at any $\Delta\tilde{\rho}$ form short tubes as a result of scrolling along the longitudinal direction of the layer. By design, however, the layer-anisotropy-driven and the defect-pattern-driven curve formation in Model PL-H compete with each other, causing uncertainty in the scroll direction. For the same reason, the cavity diameter is rather difficult to control despite the regularity of the defects of Model PL-H. At a glance, it was anticipated that the layer anisotropy governs the rolling process at low $\Delta\tilde{\rho}$ values, making the sheet curve along the longitudinal direction. As $\Delta\tilde{\rho}$ increases, the effect of the defect pattern becomes dominant and the sheet folds along the lateral direction. Nevertheless, we found that the scroll direction depends not on $\Delta\tilde{\rho}$ but on the defect width d for Model PL-H. Figure 4(c) indeed indicates that Model PL-H results in short

($d=1$), twisted ($d=2$), and long ($d\geq 3$) nanotubes depending on the graft width. In other words, when PL-H type defect grafts are used on anisotropic layers, *g*G-*d*D patterns with $d > l_g/2$, where the graft coil length is l_g, are suitable to form monodisperse nanotubes not only in terms of the internal cavity diameter but also in terms of the shape of the nanotubes.

C. Kinetics

The transformation kinetics of sheets to tubes is studied in terms of the radius of gyration, $\widetilde{R}_g(t)$. The three principal components, $\overline{R}_{\alpha\alpha}(t)$ ($\alpha = x, y, z$), and the radius of gyration, $\widetilde{R}_g(t) = \sqrt{\overline{R}_{xx}^2(t) + \overline{R}_{yy}^2(t) + \overline{R}_{zz}^2(t)}$, are obtained from the radius of gyration tensor. Its elements are defined as

$$R_{\gamma\delta} = \frac{1}{M_{layer}} \sum_{i=1}^{M_{layer}} (\gamma_i - \gamma_{CM})(\delta_i - \delta_{CM}), \tag{5}$$

where γ_i and δ_i are the *x*, *y*, and *z* coordinates of the i^{th} bead of the layer. γ_{CM} and δ_{CM} are those of the center of mass of the layer consisting of M_{layer} beads. In Figure 5, the black dashed lines represent $\widetilde{R}_g(t)$ and the colored solid lines denote the three principal components, $\overline{R}_{\alpha\alpha}(t)$. In particular, the red lines describe the time evolution of the longitudinal dimension of the sheet. Initially, the longitudinal component of all sheets is identical to the long edge of the sheet, and it decreases as the sheet scrolls. Due to the randomly distributed point defects, the kinetics of Model RP varies arbitrarily and markedly depending on the defect distribution at a given value of $\Delta\widetilde{\rho}$, whereas the scroll direction is always along the longitudinal side of the sheet, even for twisted ones.

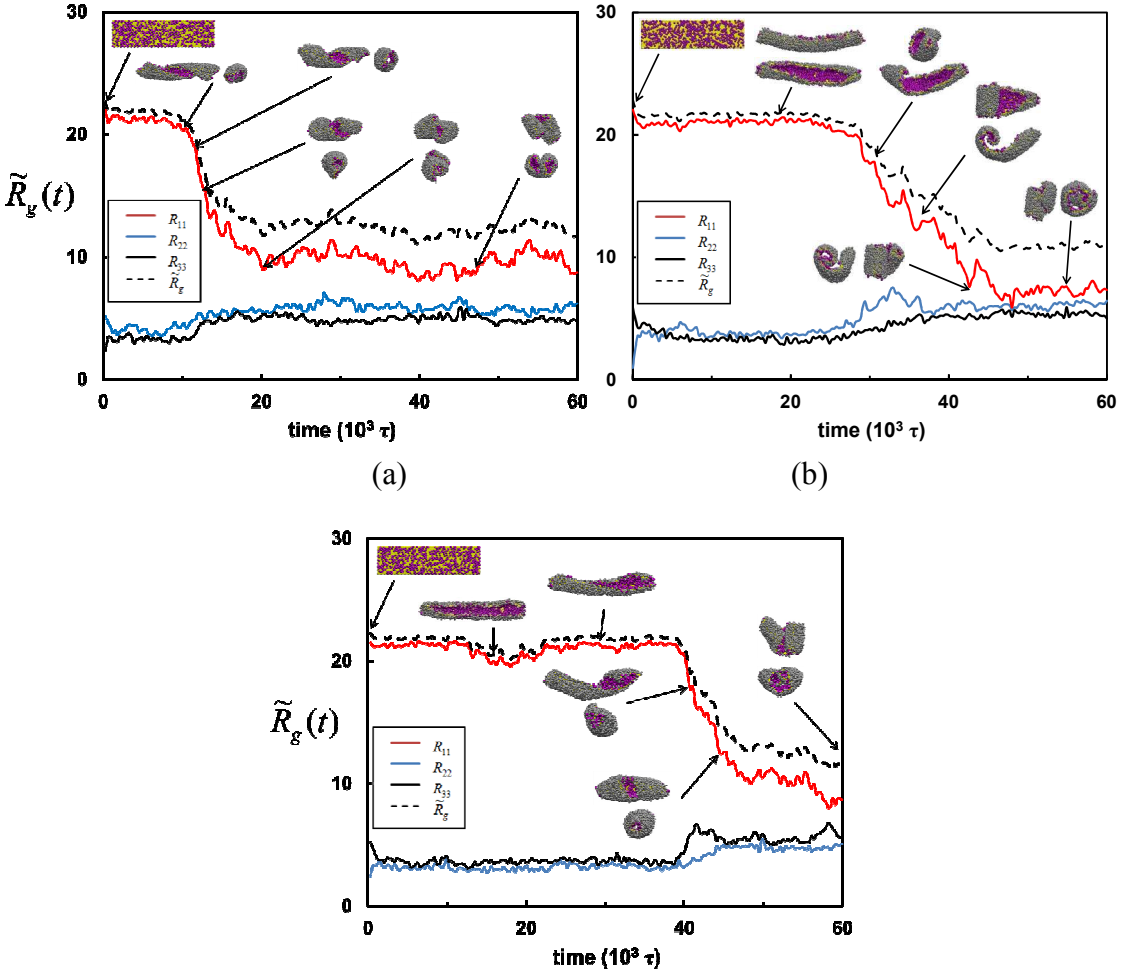

Figure 5. Time evolution of the radius of gyration of Model RP. These correspond to the three random defect distributions in Fig. 2 when $\Delta\widetilde{\rho} = 0.48$.

Regular defect patterns help control the kinetics of the tube transformation, for which the curve formation rate can be controlled by the patterned defect. Also, Fig. 6 shows that a higher curve transformation rate leads to a smaller internal cavity. As demonstrated in Fig. 6(c), we defined the initial scroll rate as the linear regression slope of $\widetilde{R}_g(t)$ during an early trajectory. The early stage of simulation includes the initial time-evolution until $\widetilde{R}_g(t)$ stops from a rapid decrease and reaches near plateau-like limit. The driving force of the curve formation varies with respect to $\Delta\widetilde{\rho}$; at a high $\Delta\widetilde{\rho}$, the rolling of

the sheet is driven by graft defects; therefore, the rate varies greatly in relation to the defect width. However, at a low value of $\Delta\tilde{\rho}$, the curve formation is mainly governed by layer anisotropy such that the rate is less sensitive to the graft defect. The change in the rate when we vary the defect width from $d = 2$ to $d = 3$ increases 10 times at $\Delta\tilde{\rho} = 0.40$ compared to that at $\Delta\tilde{\rho} = 0.18$.

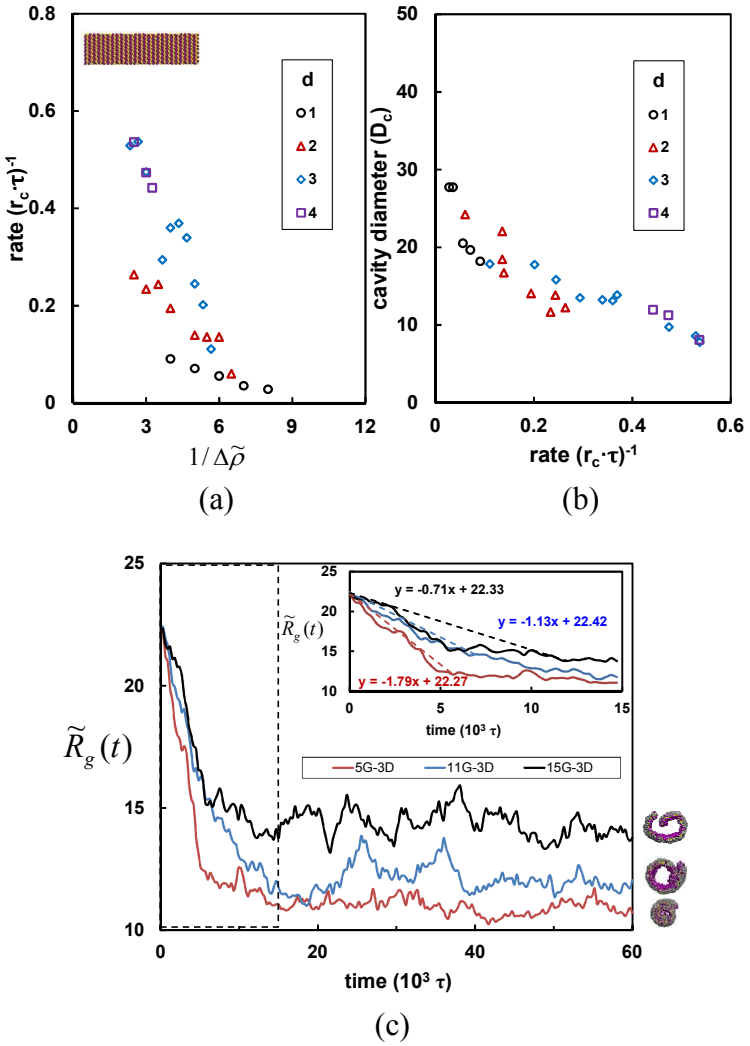

Figure 6. Initial scroll rate of Model PL-V for rectangular nanosheets with respect to (b) the graft-defect density ($\Delta\tilde{\rho}$) and (c) the cavity diameter (D_c). Here, (c) presents the relationship between the initial scroll rate and the radius of gyration.

To provide a realistic and quantitative estimation of the size of the nanotubes and the self-rolling process time rates, we converted DPD units to the physical length and time scale. First, we assumed that one coarse-grained bead contains three water molecules with a volume of 90 Å^3. By applying the physical length and time scale matching technique,[35] the length and time unit correspond, respectively, to $r_c = 6.46$ Å and $\tau = 88.0$ ps. When this scale is applied to Fig. 5, the diameter (length) of the nanotubes is approximately 6.5 nm (13.0 nm) and the self-rolling occurs within 5 μs, a feasible drug carrier size and feasible time range.[26] Applications of the findings in this work with regard to the surface-modification technique are not limited to nanometer-scale tubes; application is also possible with micrometer-sized structural fabrication. The dimensions of drug carriers that are currently under investigation span a wide length range, roughly from 20 to 600 nm.[26] An advantage of the theoretical studies performed here is that the findings are applicable to any regime of length scale as long as a quantum mechanical effect does not play a role. Using the technique introduced here, tuning the dimension of the carrier for proper targeting usage can be readily accomplished by altering not only the physical dimensions of the components but also the intrinsic properties of the layer and the graft coils.

Assuming that we employ a biodegradable polymer such as poly(lactic acid) (PLA) or poly(lactic-co-glycolic acid) (PLGA) as ***R***- and ***D***-coils of a drug carrier; due to their biocompatibility, such polymers are considered as a promising resource for drug carriers. Within the cell environment, ***R***-coils that cover the exterior of the carrier begin to dissolve, and eventually the scrolled tubes unfold and expose the drugs deposited in the interior. To mimic the hydrolysis of graft coils, we detached randomly chosen grafted ***R***-coils and followed the progress of the unfolding process shown in Fig. 7. With the Model PL-V sheet with the 11G-3D pattern when $\Delta\tilde{\rho} = 0.21$, hydrolyzed ***R***-coils of 10%, 21% and 50% cases were studied. Whereas, 10% hydrolysis leads to no structural transition, the nanotube inverts completely if half of the ***R***-coils are dissolved.

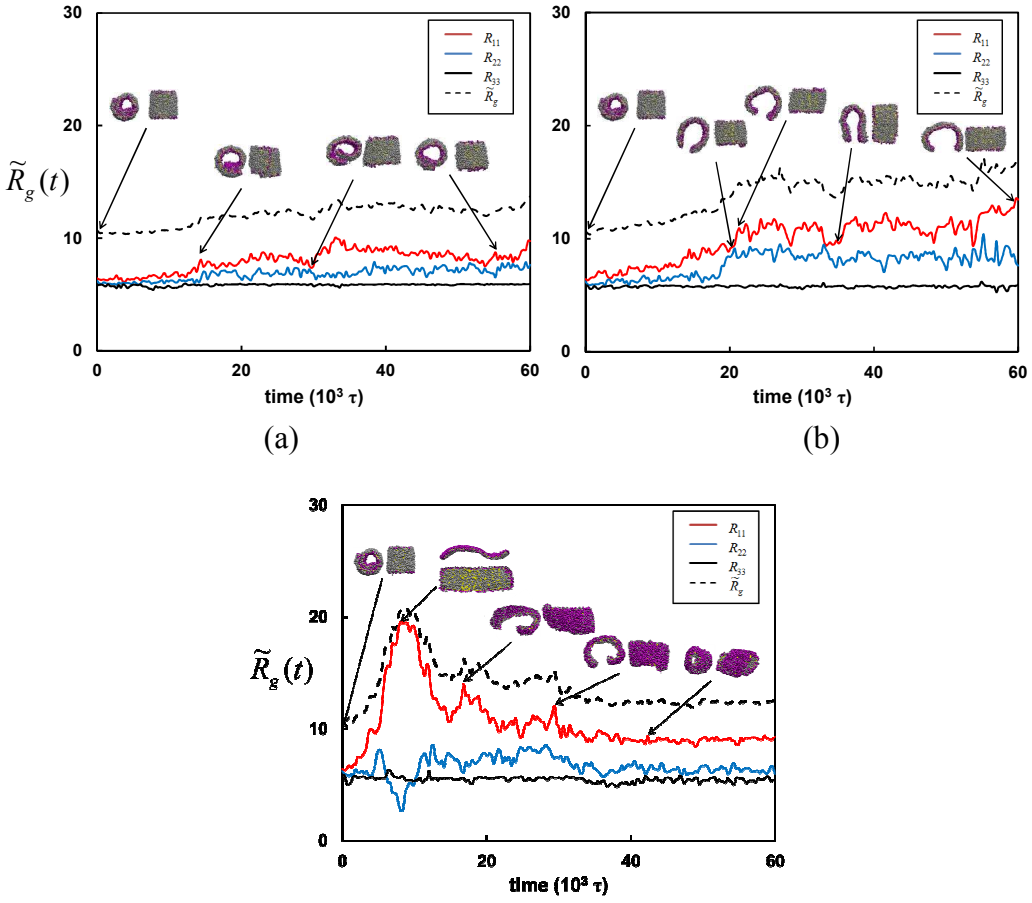

Figure 7. Unfolding of Model PL-V by the dissolution of (a) 10%, (b) 21%, and (c) 50% ***R***-coils with the 11G-3D pattern when $\Delta\tilde{\rho} = 0.21$. Time evolution values of the radius of gyration are presented along with cross-sectional and side views of the tubes.

D. Faceted Nanotubes

An advantage of employing a patterned defect is that it also becomes possible to control the shape of the cross-sections. Given the folding-like conformation of wide-defect-pattern models, one can also produce hollow cylinders with polygon-like cross-sections, as shown in Fig. 8. By manipulating the defect patterns, various polygonal nanotubes, including triangular, square, pentagonal, and hexagonal nanotubes, were successfully formed. In addition to the numerous mechanisms which can be used to

realize self-folding inorganic materials,[31] this work presents a new paradigm in the control of faceted organic nanotubes. Although most lipid bilayer vesicles or tubes have smooth and round surfaces in biological systems, one often observes faceted structures as well. Examples are protein capsids of many large viruses, the protein-enclosed bacterial organelles known as carboxysomes, and the square-shaped bacteria found in saturated brine pools.[32] These faceted biomaterials have different Brownian motions and surface functionalities as compared to their round counterparts, as the number of facets and their polygonal shape play crucial roles in micro-systems. The surface graft modification technique will also provide a tool with which to form faceted organic nanotubes, which may be used as part of an artificial cell component.

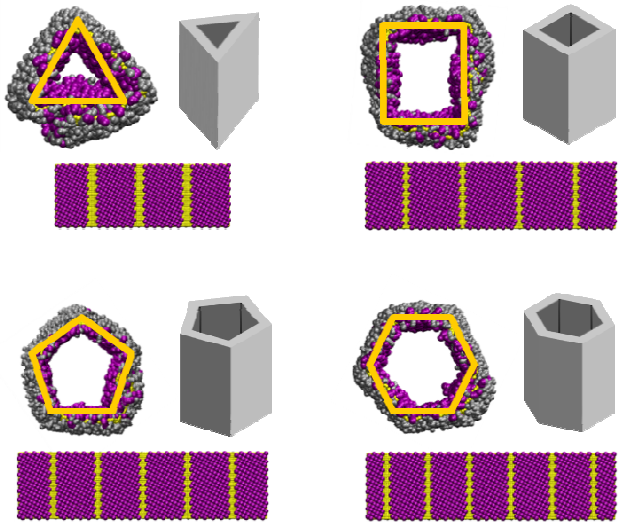

Figure 8. Cross-sectional views of hollow polygonal nanotubes and corresponding initial graft-defect patterns. To induce the sharp edges of the polygonal cross-section, *g*G-*d*D (d = 6 for the triangular nanotube; d = 4 for the rest, $24 < g < 30$ depending on the side length of polygons) patterns of Model PL-V were used.

IV. CONCLUDING REMARKS

Utilizing DPD simulations of coarse-grained sheet models, we show that the internal cavity size of nanotubes can be controlled by regulating the surface graft defects of a lyophobic sheet. In addition, we have shown that the scrolling direction can be controlled by the type of graft-defect pattern used. At any graft-defect density, Models RP and PL-V scroll along the longitudinal edges. In contrast, depending on the defect width, Model PL-H scrolls along either the lateral or the longitudinal direction due to the conflict between the layer anisotropy and the graft-defect pattern. When the defect width is narrow, the overall scrolling occurs along the longitudinal direction owing to layer anisotropy. However, when the width of the graft defect is sufficiently large, the scrolling directing is determined by the graft defects. For the rectangular nanosheets used here, a defect pattern wider than half of the graft chain length governs the scroll direction. In summary, to produce hollow nanotubes with wide range of internal cavities systematically, the narrow defect pattern of Model PL-V is suitable. To produce monodisperse hollow nanotubes for a given internal cavity and a wide defect pattern wider than half of the graft coil length, of Model PL-V works best. Regardless of the pattern of the graft defects, the graft-defect density governs the internal cavity diameter. For patterned defect models, the width of the defect pattern determines the kinetics of curve formation. This work offers scientific insight into nanotube fabrication via surface modification by providing a substantial understanding of the manipulation of graft defects and the role of the graft pattern on secondary architecture types.

ACKNOWLEDGMENT This work was supported by grants from the National Research Foundation (2012R1A1A2004782 and 2012M3C1A6035358) and the project EDISON funded by the Korean government and by the Yonsei Future-Leading Research Initiative (2014-22-0169). J.H. and M.W. thank the fellowship of the BK21-plus program from MOEHRD.

FIGURE CAPTIONS

Figure 1. Initial grafts and time evolution of the spontaneous curvature formation of 4:15 rectangular nanosheets at various graft-defect densities, $\Delta\tilde{\rho}$. The defect-free nanosheet in (a) and the random point defect models (Model RP) in (b) are shown, with $\Delta\tilde{\rho} = 0.15$ (c) $\Delta\tilde{\rho} = 0.27$, and (c) $\Delta\tilde{\rho} = 0.48$. In the initial grafts, purple points represent coil grafted points, while yellow layer beads are exposed at defect sites. At other time points, cross-sectional views of the sheet are shown. For a given $\Delta\tilde{\rho}$, three uncorrelated randomly distributed defect models were chosen.

Figure 2. Initial graft patterns and cross-sectional views of the evolving tubes with line defect models. (a) *g*G-3D pattern of a square nanosheet, *g*G-3D patterns of (b) Model PL-V and (c) Model PL-H of a rectangular nanosheet. (d) *g*G-1D pattern of Model PL-H of a rectangular nanosheet. In the initial grafts, purple points denote coil grafted sites, while yellow layer beads are exposed at the defect sites.

Figure 3. Relationship between the graft-defect density ($\Delta\tilde{\rho}$) and the cavity diameter (D_c): (a) Model PL-V, (b) Model RP, and (c) Model PL-H of a rectangular nanosheet, (d) Model PL of a square nanosheet. Here, (e) visualizes the relationship between D_c and the cross-section of the nanotubes. Schematically, (f) shows how to determine the average and the standard deviation of the cavity diameter, e.g., when $\Delta\tilde{\rho} = 0.25$. Values in legends are *d* values of the gG-dD defect models.

Figure 4. The cavity diameter as a function of the graft width, *g*, and the defect width, *d*. (a) and (b) denote the *g*G-*d*D pattern of Model PL-V, and (c) and (d) denote this for Model PL-H.

Figure 5. Time evolution of the radius of gyration of Model RP. These correspond to the three random defect distributions in Fig. 2 when $\Delta\tilde{\rho} = 0.48$.

Figure 6. Initial scroll rate of Model PL-V for rectangular nanosheets with respect to (b) the graft-defect density ($\Delta\tilde{\rho}$) and (c) the cavity diameter (D_c). Here, (c) presents the relationship between the initial scroll rate and the radius of gyration.

Figure 7. Unfolding of Model PL-V by the dissolution of (a) 10%, (b) 21%, and (c) 50% ***R***-coils with the 11G-3D pattern when $\Delta\tilde{\rho} = 0.21$. Time evolution values of the radius of gyration are presented along with cross-sectional and side views of the tubes.

Figure 8. Cross-sectional views of hollow polygonal nanotubes and corresponding initial graft-defect patterns. To induce the sharp edges of the polygonal cross-section, *g*G-*d*D (d = 6 for the triangular nanotube; d = 4 for the rest, $24 < g < 30$ depending on the side length of polygons) patterns of Model PL-V were used.

TABLES AND SCHEMES

Scheme 1. Top and side views of the initial graft models of a rectangular nanosheet along with the layer-bead (yellow beads) arrangement and their bonding scheme. (a) ***R***-coil (reference side, gray beads) grafts and ***D***-coil (defect side, purple beads) grafts of (b) random point defects (Model RP), (c) patterned vertical line defects (Model PL-V), and (d) patterned horizontal line defects (Model PL-H). For (b) to (d), the graft-defect density, $\Delta\widetilde{\rho} = 0.32$, was chosen for illustration. As shown in (c), the notation *g*G-*d*D denotes the repeating pattern consisting of *g* grafted points followed by missing *d* graft points.

Table 1. DPD potential parameters: repulsion parameter ($a_{\alpha\beta}$), bonding force constant (k), and equilibrium bond distance ($\overline{r}$). In subscripts *N*, *R*, *D*, and *S* represent, respectively, the nanolayer, reference and defect coil, and the solvent beads. $a_{\alpha\beta}$ is in units of $k_B T$.

REFERENCES

1. J. M. C. A. S. Rudolph, P. E. Schoen, J. M. Schnur, B. P. Gaber, D. Chapmen, *Biotechnological Application of Lipid Microstructures*, Plenum, New York, 1988.
2. S. Iijima, *Nature*, 1991, **354**.
3. B. Wang, C. H. P. Poa, L. Wei, L.-J. Li, Y. Yang and Y. Chen, *J. Am. Chem. Soc.*, 2007, **129**, 9014-9019.
4. T. Shimizu, *J. Polym. Sci., Part A: Polym. Chem.*, 2006, **44**, 5137-5152.
5. C. Tarabout, S. Roux, F. Gobeaux, N. Fay, E. Pouget, C. Meriadec, M. Ligeti, D. Thomas, M. IJsselstijn, F. Besselievre, D.-A. Buisson, J.-M. Verbavatz, M. Petitjean, C. Valéry, L. Perrin, B. Rousseau, F. Artzner, M. Paternostre and J.-C. Cintrat, *Proc. Natl Acad. Sci.*, 2011.
6. H. Jin fan, M. Knez, R. Scholz, K. Nielsch, E. Pippel, D. Hesse, M. Zacharias and U. Gosele, *Nat. Mater.*, 2006, **5**, 627-631.
7. S. J. Son, X. Bai, A. Nan, H. Ghandehari and S. B. Lee, *J. Controlled Release*, 2006, **114**, 143-152.
8. Z. Leila, *J. Controlled Release*, 2002, **81**, 7-23.
9. E. Lee, J.-K. Kim and M. Lee, *Angew. Chem. Int. Ed.*, 2009, **121**, 3711-3714.
10. Y. D. Li, X. L. Li, R. R. He, J. Zhu and Z. X. Deng, *J. Am. Chem. Soc.*, 2002, **124**, 1411-1416.
11. H. J. Fan, U. Gösele and M. Zacharias, *Small*, 2007, **3**, 1660-1671.
12. L. Radzihovsky and J. Toner, *Phys. Rev. Lett.*, 1995, **75**, 4752-4755.
13. M. Bowick, M. Falcioni and G. Thorleifsson, *Phys. Rev. E*, 1997, **79**, 885-888.
14. O. Stenull, *Phys. Rev. E*, 2008, **78**, 031704.
15. B. K. Mishra and B. N. Thomas, *J. Am. Chem. Soc.*, 2002, **124**, 6866-6871.
16. D. L. Johnson, N. A. Esmen, K. D. Carlson, T. A. Pearce and B. N. Thomas, *J. Aerosol. Sci.*, 2000, **31**, 181-188.
17. M. Iyoda, M. Hasegawa and H. Enozawa, *Chem. Lett.*, 2007, **36**, 1402-1407.
18. X. Chen and S. S. Mao, *J. Nanosci. Nanotechno.*, 2006, **6**, 906-925.
19. Z. Wang and M. Brust, *Nanoscale Res. Lett.*, 2006, **2**, 34-39.
20. Z. Liu, D. Zhang, S. Han, C. Li, B. Lei, W. Lu, J. Fang and C. Zhou, *J. Am. Chem. Soc.*, 2004, **127**, 6-7.
21. L. Zhao, M. Yosef, E. Pippel, H. Hofmeister, M. Steinhart, U. Gösele and S. Schlecht, *Angew. Chem. Int. Ed.*, 2006, **45**, 8042-8045.
22. X. W. Lou, D. Deng, J. Y. Lee, J. Feng and L. A. Archer, *Adv. Mater.*, 2008, **20**, 258-262.
23. Z. Wang, C. J. Medforth and J. A. Shelnutt, *J. Am. Chem. Soc.*, 2004, **126**, 15954-15955.
24. J. C. Mitchell, J. R. Harris, J. Malo, J. Bath and A. J. Turberfield, *J. Am. Chem. Soc.*, 2004, **126**, 16342-16343.
25. R. Iwaura and T. Shimizu, *Angew. Chem. Int. Ed.*, 2006, **45**, 4601-4604.
26. S. Vauthey, S. Santoso, H. Gong, N. Watson and S. Zhang, *Proc. Natl. Acad. Sci. USA*, 2002, **99**, 5355-5360.
27. R. Tenne, L. Margulis, M. Genut and G. Hodes, *Nature*, 1992, **360**, 444-446.
28. G. Radovsky, R. Popovitz-Biro, M. Staiger, K. Gartsman, C. Thomsen, T. Lorenz, G. Seifert and R. Tenne, *Angew. Chem. Int. Ed.*, 2011, **50**, 12316-12320.
29. Y. M. Lvov, D. G. Shchukin, H. Möhwald and R. R. Price, *ACS Nano*, 2008, **2**, 814-820.
30. K. Kumar, B. Nandan, V. Luchnikov, S. Zakharchenko, L. Ionov and M. Stamm, *Mater. Res. Soc. Symp. Proc.*, 2010, **1272**.
31. M. Han and E. Sim, *J. Phys. Chem. B*, 2012, **116**, 1796-1801.
32. M. Han and E. Sim, *J. Phys. Chem. B*, 2012, **116**, 5771-5776.
33. M. Han, J. Hyun and E. Sim, *J. Phys. Chem. B*, 2013, **117**, 7763-7770.

34. M. Steenackers, A. M. Gigler, N. Zhang, F. Deubel, M. Seifert, L. H. Hess, C. H. Y. X. Lim, K. P. Loh, J. A. Garrido, R. Jordan, M. Stutzmann and I. D. Sharp, *J. Am. Chem. Soc.*, 2011, **133**, 10490-10498.
35. R. D. Groot and K. L. Rabone, *Biophys. J.*, 2001, **81**, 725-736.
36. K. H. Hsu, P. L. Schultz, P. M. Ferreira and N. X. Fang, *Nano. Lett.*, 2007, **7**, 446-451.
37. K. Salaita, Y. Wang and C. A. Mirkin, *Nat. Nano.*, 2007, **2**, 145-155.
38. C. L. Haynes and R. P. Van Duyne, *J. Am. Chem. Soc.*, 2001, **105**, 5599-5611.
39. D. Frenkel and B. Smit, *Understanding Molecular Simulation*, Academic Press, Dan Diego, 2002.
40. P. Español and P. Warren, *Europhys. Lett.* , 1995, **30**, 191.
41. R. D. Groot and P. B. Warren, *J. Chem. Phys.*, 1997, **107**, 4423-4435.
42. http://lammps.sandia.gov.
43. W. Humphrey, A. Dalke and K. Schulten, *J. Mol. Graphics*, 1996, **14**, 33-38.